J. Indian Inst. Sci.
A Multidisciplinary Reviews Journal
ISSN: 0970-4140 Coden-JIISAD

REVIEW ARTICLE

Secondary Breakup of Drops

*R Suryaprakash and Gaurav Tomar**

Abstract | Secondary atomization of droplets generated from primary atomization is observed in high-speed flows. In natural scenarios, falling raindrops undergo aerodynamic breakup that modifies the resulting drop size distribution on the ground. In this article, we review some aspects of the drop breakup mechanisms, initial deformation, drag characteristics, and time scales of breakup. We also review some of the secondary atomization models, such as TAB and DDB, proposed in the literature. We discuss the role of new numerical algorithms for two-phase flow simulations in providing insights into the exact physical mechanisms involved during drop breakup.

1 Introduction

Secondary atomization is the breakup of liquid drops from primary atomization further into smaller fragments. This can occur due to high-speed ambient flow over the drops, such as in gas turbine combustion engines, or due to the high speed of the drops in an otherwise quiescent ambient fluid as observed in sprays and falling raindrops. In combustion chambers, primary atomization often yields a fraction of the droplets that are susceptible to further breakup[1,2]. Secondary breakup is observed in liquid atomization, sprays in cosmetic, chemical and drying industries, agricultural sprays, and gas–liquid separators. In geological flows, liquid drops formed in clouds attain a critical size at which they can no longer be levitated by the convective upward draft and turbulent flow in clouds, and thus, they fall. As they fall, they agglomerate more drops and become even bigger. Due to the high falling terminal speeds, surface tension can no longer hold the drop together and it fragments by secondary atomization mechanisms[3,4].

In the last few decades, secondary breakup has received a lot of attention due to the drive towards more efficient atomization systems for gas turbine engines. Several review articles on secondary atomization have been written periodically[5–11]. The latest of the review article[10] discussed in detail the different modes of drop breakup and the possible mechanisms proposed to explain them. The mode that a drop breaks up in is a function of the relative velocity between the drop and the ambient fluid. At low speeds, in a shear flow, continuous action of the shear forces can overcome the restoring surface tension forces and lead to its breakup. The fragments that the drop breaks up into are few. Breakup of the drop due to the shear forces is characterized by the capillary number $Ca = \mu_g U_0/\sigma$, where μ_g is the viscosity of the ambient fluid, U_0 is velocity of the ambient flow, and σ is the surface tension coefficient. At higher speeds, inertial forces deform the drop and lead to its breakup and it is characterized by the aerodynamic Weber number $We = \rho_g U_0^2 D_0/\sigma$, where ρ_g is the density of the ambient fluid and D_0 is the diameter of the drop. Shear breakups are normally observed in narrow channel flow, where the shear is strong at the length scale of the drop, whereas inertial breakup of the drop occurs in natural scenarios such as falling rain drops and in combustion chamber, where the flow speeds are high. At moderate *We*, bag breakup is observed, where the drop deforms into a bag and then fragments into very tiny droplets.

At higher *We*, shear stripping mode is observed, where the droplet is sheared at the periphery and the edge of the droplet is stretched into ligaments that keep yielding small droplets. At very high $We > 200$, catastrophic breakup is observed and the entire droplet undergoes

Department of Mechanical Engineering, Indian Institute of Science Bangalore, Bangalore, India.
**gtom@iisc.ac.in*

Springer IISc Press

Table 1: Breakup regimes as reported in literature.

Breakup regime	Pilch and Erdman[7]	Krzeczkowski[8]	Chou et al.[12]	Guildenbecher et al.[10]	Jain et al.[13]
Vibrational or no breakup	$We < 12$	$We < 10$		$We < 11$	$We < 12$
Bag	$12 < We50$	$10 < We < 18$	$13 < We < 20$	$11 < We < 35$	$12 < We < 24$
Bag-stamen	$50 < We < 100$	$18 < We < 30$		(Multimode) $35 < We < 80$	$24 < We < 45$
Bag/plume					$45 < We < 65$
Multi-bag					$65 < We < 85$
Shear				$80 < We < 350$	$We > 85$
Catastrophic				$350 < We$	

breakup at considerably small time scales. Dependence on other non-dimensional parameters, such as liquid Ohnesorge number Oh_l, is weak for lower values of Oh_l. Liquid Ohnesorge number relates the viscous forces to inertial and surface tension forces, $Oh_l = \mu_l/\sqrt{\rho\sigma D_0}$, where μ_l is the viscosity of the liquid. Krzeczkowski[8] presented a phase plot to indicate the transition Weber and Ohnesorge numbers for different modes. Brodkey also proposed the correlation (see Fig. 1):

$$We_c = We_{c,Oh\to 0}(1 + 1.077Oh_l^{1.6}). \quad (1)$$

Figure 1 shows that at Ohnesorge numbers less than 0.1, the transition We is independent of Oh_l and varies considerably beyond 0.1. Clearly, at high Oh_l that is for very viscous fluids, the required Weber number increases drastically. The $We_{c,Oh\to 0}$ values used are obtained from Guildenbecher et al.[10]. Table 1 shows the different transition Weber numbers. The variation between the different studies is considerable and has mostly been attributed to some variations in liquid/gas properties. Although experimental techniques have been extensively used to study secondary atomization, little information has been obtained on the flow features around the droplet during the breakup process. Most of the experimental studies have focused on the drop deformation and breakup characteristics. A few studies have also performed a detailed analysis of breakup times[9, 12, 14]. However, details of the initial deformation of the drop and the associated time scales have been neglected in previous studies. Robust numerical simulations provide detailed flow features around the droplet and thus are more reliable in revealing the mechanisms behind the different modes of breakup[13, 15–17].

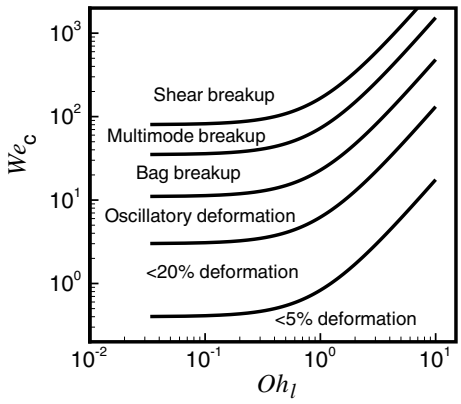

Figure 1: Correlation between the critical Weber number and liquid Ohnesorge number based on the expression given by Brodkey[18].

However, most numerical simulations of drop breakup physics have been performed at low-density ratios (10–100)[15, 17, 19–22]. Recently, Jain et al.[13] presented detailed three-dimensional simulations of drop breakup at a density ratio of 1000. Xiao et al.[16] also presented three-dimensional simulations using a CLSVOF algorithm in the high We regime. Several key features of bag formation are quite different between the low- and high-density ratio simulations. The rim of the bag is much thicker in the low-density ratio simulations, also bag-with-stamen mode is not clearly observed in these simulations[15, 20], whereas in high-density ratio, simulations bag features observed in experiments are quite accurately captured. In any case, the low-density ratio simulations are useful in understanding of formation of solid pellets by quenching. Heavy liquid metal drops falling into another lower density liquid (mercury/water) are low-density ratio systems ($\sim$ 10) and have been

studied both experimentally[23] and theoretically[24, 25].

In the present article, we review the key aspects of secondary atomization. We discuss the different modes of breakup of drops at different aerodynamic Weber numbers. Experimental and numerical simulations for the initial deformation of the drop, drag coefficients, and time scales of deformation and breakup have been discussed. We also present some key issues such as inconsistency in the transition Weber number from various studies as well as effects of density ratio, viscosity ratio, and gas Reynolds number that can explain the discrepancies. This paper is organized as follows. The section on problem description describes the experimental and numerical setups employed in the literature to study secondary atomization. In the numerical modeling section, we discuss various models, used extensively by the spray modeling community, and their limitations. Subsequently, we discuss initial drop deformation, drag coefficient, and time scales of deformation and breakup. Different breakup modes and issue of transition Weber numbers is discussed in Sect. 5. Finally, we present summary and some future directions.

2 Problem Description

Droplet breakup depends on the relative strengths of the various forces acting on it. In low speed flows, the integrity of the droplet is lost when the shear forces are relatively stronger than the capillary forces[26–28]. Breakup of a drop in natural settings such as in falling drops from clouds depends on the aerodynamic Weber number based on the terminal velocity of the drop and the Ohnesorge number[5, 10, 29, 30]. In industrial applications, such as in gas turbines and other combustion engines, droplets emerging from the primary atomization are subjected to high-speed crossflow and thus may further fragment depending upon the aerodynamic Weber number for the drop based on the crossflow velocity and the diameter of the droplet[31–33] .

To study the sudden breakup of drops by aerodynamic forces, a droplet can be suspended in a shock tube and subjected to a shock flow generated by breaking a diaphragm and releasing highly pressurised gas in the tube. The shock passes over the droplet without causing any significant deformation and the droplet breaks up due to the convective flow upstream of the shock. The drop is essentially subjected to a sudden acceleration and the flow configuration is more amenable to theoretical analysis[34], as noted in Guildenbecher et al.[10]. Thus, majority of the earlier experiments were performed in shock tubes (see[5, 9, 12, 35–42]). Some of the more recent studies have been performed by allowing the droplets to flow through a continuous stream of flow through a nozzle (see[43–47]). Of course, care needs to be taken to obtain a uniform profile with thin shear layers and ensure that the droplet enters the uniform velocity region before undergoing any deformation or momentum exchange with the crossflow in the shear layer region. Guildenbecher et al.[10] provide a time scale analysis to determine the falling speeds of the droplet relative to the crossflow to minimize the above effects. One can also do experiments in drop towers, but diagnostics becomes difficult and also direct applicability of such studies is limited to natural scenarios such as falling rain drops.

Numerical modeling of secondary breakup has mostly involved Lagrangian particle tracking with local breakup models such as the Taylor Analogy Breakup (TAB)[48], Clark model[49] and the Droplet Deformation Breakup (DDB)[50]. TAB model is essentially based on the deformation of the droplet into an oblate shape. A simplistic mass-spring-damper system forced by the dynamical forces is used to estimate the drop deformation in the equatorial direction (x denotes the displacement at the pole with respect to spherical drop):

$$m\ddot{x} = F - kx - d\dot{x}. \tag{2}$$

Here, the forcing function is given by $F = C_F m\rho_g U^2/\rho_l d_0$, where U is the mean velocity of the ambient fluid, d_0 is diameter of the undeformed droplet, ρ_g is the density of the ambient gas, and ρ_l is the density of the drop liquid. The coefficient is $C_F = 2/3$. The spring force models the capillary force using a spring constant $k = C_k m\sigma/\rho_l d_0^3$ with $C_k = 64$. The damping force represents the viscous effect $d = C_d m\mu_l/\rho_l d_0^2$, where $C_d = 20$. The above equation can be further re-organized and written in terms of the non-dimensional terms using $x^* = x/d_0$ and time $t^* = d_0/U$:

$$\ddot{x^*} + C_d \frac{M}{Re\rho*}\dot{x^*} + \frac{C_k}{We\rho*} = \frac{C_F}{\rho*}. \tag{3}$$

Here, $M = \mu_l/\mu_g$ is the ratio of the viscosities, $rho* = \rho_l/\rho_g$ is the ratio of densities, $Re = \rho_g U d_0/\mu_g$ is ambient gas Reynolds number and $We = \rho_g U^2 d_0/\sigma$ is the aerodynamic Weber number. The solution to the above equation essentially indicates the amplitude of oscillation of the droplet and using a criterion that the droplet breaks when the deformation x is one-fourth

of the diameter of the droplet. TAB model works accurately in the Weber number regime, where vibrational breakup is expected. The size and velocity of the daughter droplet are obtained using energy considerations[48]. Another variant of the TAB model is the Improved TAB (I-TAB) model[51], where even the change in drag force with drop shape is considered. The DDB model on the other hand is based on energy takes into account the non-linear effects that become active at large deformations. Considering the rate of work done by pressure and viscous forces and balancing it with the kinetic energy and the surface tension energy, a differential equation is obtained for the displacement of the pole relative to the spherical undeformed drop. Interestingly, Lee et al.[52] concluded that DDB model is erroneous and shows no improvement over the TAB model. A non-linear version of TAB (NL-TAB) has also been proposed to account for the different modes of breakup[53]. There are some other secondary droplet models also that have been proposed based on empirical correlations for breakup times and size distributions[7, 54, 55]. At higher Weber numbers, where several other hydrodynamic instabilities become active, several breakup models have been proposed such as Reitz's wave breakup[56]. Enhanced-TAB[57] and Cascade Atomization Breakup (CAB)[58] models modify the TAB model to account for the high Weber number effects.

Apte et al.[59, 60] proposed a stochastic subgrid breakup models that uses a Fokker–Planck formulation for the evolution of size distribution of the drops. Recently, a more detailed model based on virtual work principle for bag breakup regime has been proposed by Sichani and Emami[61].

The applicability of the above-discussed secondary breakup models is limited to a regime of breakup or the other and detailed numerical simulation are required to be performed to understand the fragmentation process. Direct numerical simulations to study secondary breakup regime have also been actively pursued in the last decades. Front tracking, Level Set, VOF, and Coupled Level Set VOF have been employed by different groups with different degrees of success for different breakup regimes. These methods are one-fluid models, where the liquid and gas are treated as a single inhomogeneous incompressible fluid. Here, we will discuss briefly the Level Set and VOF methods. The governing equations for momentum and mass conservation are given by

$$\nabla \cdot \mathbf{u} = 0, \tag{4}$$

where $\mathbf{u}$ is the divergence free velocity field. The governing equations for the momentum conservation are given by the Navier–Stokes equations (Eq. 5) modified to implicitly account for the surface tension forces and the interfacial boundary conditions of continuity of velocity, and normal and tangential stress balance:

$$\rho(C)\left(\frac{\partial \mathbf{u}}{\partial t} + \nabla \cdot \mathbf{uu}\right) = -\nabla p + \nabla \cdot (2\mu(C)\mathbf{D}) + \sigma\kappa\mathbf{n}\delta_s. \tag{5}$$

Here, C is the indicator function that takes a value of zero in the gas phase and one in the liquid phase. The density and viscosity for the one-fluid formulation are expressed as, $\rho = \rho_l C + \rho_g(1-C)$ and $\mu = \mu_l C + \mu_g(1-C)$, respectively. The deformation rate tensor is given by $D = (\nabla\mathbf{u} + (\nabla\mathbf{u})^{\mathrm{T}})/2$. The last term in the equation ($\sigma\kappa\mathbf{n}\delta_s$) accounts for the surface tension force ($\sigma\kappa$, where κ is the local interface curvature) acting on the interface, expressed as a volumetric force using the surface Dirac delta function (δ_s) and modeled using the continuum surface force approach[62]. The direction of this force is along the local normal ($\mathbf{n}$) at the interface.

The indicator function is represented by a signed distance function ϕ in Level set method, whereas in volume of fluid methods, the fraction of the volume of liquid in a grid cell (F) is used. The evolution equation for both the level set function as well as the void fraction is obtained by applying the kinematic boundary condition at the interface:

$$\frac{\partial C}{\partial t} + \mathbf{u} \cdot \nabla C = 0. \tag{6}$$

Although the analytical form of the above equation is similar, it is solved algebraically in Level set methods using higher order upwind schemes or ENO schemes, whereas in VOF methods, the fluxes are computed geometrically thus ensuring strict mass conservation.

Interfacial properties such as normal and curvature are computed accurately in the Level set method as

$$\mathbf{n} = \frac{\nabla\phi}{|\nabla\phi|} \tag{7}$$

$$\kappa = -\nabla \cdot \left(\frac{\nabla\phi}{|\nabla\phi|}\right) \tag{8}$$

In VOF methods, height function approach yields a similar second order accuracy for curvature calculation except that in certain situations it fails and a more expensive parabolic reconstruction is required[63, 64].

Different schemes have been employed to numerically discretize the above equation, mostly in the finite volume/difference framework. We present below, briefly, numerically scheme used in Gerris[63] employed by[13,65]. Gerris allows use of an adaptive mesh refinement (AMR) to reduce the computational cost using a fine mesh only in regions, where either the flow structures are fine or the liquid–air interface is present.

Navier–Stokes equations are discretized and are solved implicitly using a projection method. Dropping the pressure terms from the Navier–Stokes equations, first, an auxiliary velocity field is obtained[66]:

$$\rho_{n+\frac{1}{2}}\left(\frac{\mathbf{u}_* - \mathbf{u}_n}{\nabla t} + \mathbf{u}_{n+\frac{1}{2}} \cdot \nabla \mathbf{u}_{n+\frac{1}{2}}\right) = \nabla \cdot (\mu_{n+\frac{1}{2}}(\mathbf{D}_n + \mathbf{D}_*)) + (\sigma \kappa \delta_s \mathbf{n})_{n+\frac{1}{2}}. \tag{9}$$

Then, the void fraction is obtained using the following equation:

$$\frac{C_{n+\frac{1}{2}} - C_{n-\frac{1}{2}}}{\Delta t} + \nabla \cdot (C_n \mathbf{u}_n) = 0. \tag{10}$$

The fluxes in the above equation are computed geometrically (see[63]).

A geometric multigrid method is used to solve the pressure Poisson equation:

$$\nabla \cdot \left(\frac{\nabla p}{\rho(C)}\right) = \frac{\nabla \cdot \mathbf{u}_*}{\Delta t}. \tag{11}$$

Finally, the auxiliary velocity field is corrected to obtain the divergence free velocity field at the $(n+1)th$ time step using the following equation:

$$\mathbf{u}_{n+1} = \mathbf{u}_* - \frac{\Delta t}{\rho_{n+\frac{1}{2}}} \nabla p_{n+\frac{1}{2}}. \tag{12}$$

Convergence of the direct simulations for the drop breakup case is slow and the required grid size is extremely small. Here, in Table 2, we compare some of the grid sizes used in different studies in the literature. Jalaal and Mehravan[17] employed the open-source code Gerris[66] with a very refined grid. However, the density ratio simulated was 10. Whereas, Jain et al.[13] performed simulations for a high-density ratio of 1000 with a grid refinement of $D_0/\Delta x = 200$. In most two-phase sharp interface flow simulation methods, density ratio poses severe numerical convergence restrictions. Therefore, most of the studies in the literature have been performed at low-density ratios. The convergence primarily appear due to the solution of pressure Poisson equation required in the projection schemes. We will discuss the effect of density ratio on the physics of drop breakup in a later section.

3 Initial Drop Deformation, Drag and Timescales

Lee and Reitz[67] described the initial deformation as a result of the high stagnation pressure at the equator compared to the low pressure at the pole of the drop over which the flow occurs. Hwang et al.[44] discussed drop deformation in a greater detail. They discussed drop deformation using the TAB model of[48] and the DDB model of[50]. As discussed before in the previous section, in the TAB model, the drop shape is assumed to be ellipsoidal and a simplistic spring-mass-damper model is employed to obtain the evolution of the drop in time and predict breakup. The TAB model, for the inviscid liquid case shows that the critical Weber number for breakup is 12. Breakup times determined are

$$t_{\mathrm{bu}} = \frac{\pi}{2} \Big/ \sqrt{\frac{\rho_{\mathrm{l}} D_0^3}{16\sigma}}, \tag{13}$$

where D_0 is the initial diameter of the spherical drop. Whereas, at higher We numbers, the TAB model can be used to show that the breakup time, t_{bu}, is much smaller:

$$t_{\mathrm{bu}} = \sqrt{3}\frac{D_0}{2U}\sqrt{\frac{\rho_{\mathrm{l}}}{\rho_{\mathrm{g}}}}. \tag{14}$$

Note that in the first of the above two expressions for the breakup time, gas density does not appear, since the breakup is primarily due to liquid oscillations. As indicated in previous experimental studies[6,9,35], the breakup time scale is indeed proportional to the characteristic time scale:

$$t_c = \frac{D_0}{U}\sqrt{\frac{\rho_{\mathrm{l}}}{\rho_{\mathrm{g}}}}. \tag{15}$$

However, the actual shape evolution of the drops at higher Weber numbers is quite different from the ellipsoidal shapes assumed in the TAB

Table 2: Grid sizes employed in different numerical studies.

	Zaleski et al.[19]	Han and Tryggvason[20]	Jalaal and Mehravan[17]	Jain et al.[13]
$D_0/\Delta x$	102.4	102.4	$\sim$ 1000 (AMR-effective)	$\sim$ 200
$\rho_{\mathrm{l}}/\rho_{\mathrm{g}}$	10	1/15–10	10	1000

models. Figure 2 shows the drops shapes obtained in the simulations presented in[13] for a density ratio of 1000.

These shapes are similar to the ones obtained in experiments such as those presented in Figure 2 of Ref.[35] and Figure 3 of Ref.[6]. The afghani-cap like drop shape corresponding to $We = 80$ is seen clearly in Figure 4 of Ref.[37]. The initial deformation of the droplets has been poorly discussed in the literature and the focus of most of the secondary atomization studies has been on the breakup modes that ensue once the droplet has deformed into a disk. The thickness of the disk decreases with increase in the *We* (see Fig. 2). In spite of these variations in the transient, the maximum droplet size can be predicted with reasonable accuracy, especially in the moderate Weber number regime of 20–80. In the following, we discuss development of a quasi-static model based for maximum diameter of the disk that forms at the end of the initial deformation phase of the droplet (see Jain et al.[13]).

Figure 3 shows the schematic of the oblate shaped deformed droplet. Performing a pressure balance at the equator (stagnation point) and the poles (periphery) of the droplet we can write: $p_{\text{drop}} - p_A = \sigma\kappa_A$ and $p_{\text{drop}} - p_B = \sigma\kappa_B$ which can be reduced to: $p_B - p_A = \sigma(\kappa_B - \kappa_A)$. Curvatures at the points A and B are $\kappa_A = 2D_s/D_{\max}^2$ and $\kappa_B = D_{\max}/D_s^2 + 1/D_{\max}$, respectively. Here, $D_{\max}$ is the maximum diameter The pressure difference at the points A and B would be proportional to the dynamic pressure $\rho_g U_0^2/2$: $p_B - p_A = C\rho_g U_0^2/2$. Using the volume constrained, $D_{\max}^2 D_s = D_0^3$, we obtain

$$\left(\frac{D_{\max}}{D_0}\right)^5 + \left(\frac{D_0}{D_{\max}}\right) - 2\left(\frac{D_0}{D_{\max}}\right)^4 = C\frac{We}{2}. \tag{16}$$

The above expression for $D_{\max}$ obtained above is different from the one proposed in Hsiang and Faeth[68], where $D_{max}/D_0 = 1 + 0.19We^{1/2}$. The factor 0.19 in the correlation was obtained by fitting the data. Interestingly, the roots of the Eq. (16) yield results similar to the ones obtained by the correlation proposed by[68] (see Table 3).

As the drop deforms, the drag on the drop continuously varies. Measurement of the instantaneous drag in experiments is obtained by measuring the motion of the centroid of the drop. Pilch[7] recommends the drag coefficient to be $C_d = 1.7$ in the incompressible flow regime and $C_d = 2.5$ in the compressible flow regime. Liu and Reitz[45] proposed a drag coefficient of $C_d = C_{d,S}(1 + 2.632y)$, where $C_{d,S}$ is the drag coefficient for a solid sphere and y is the distance from the deforming half droplet to its pole. Drag coefficient for a solid sphere for $Re_g > 1000$ is $C_{d,S} = 0.424$. For low-density ratio systems (liquid drops in a liquid pool), Patel et al.[23] and Baines[69] reported a drag coefficient between 2.5 and 3.0. Hsiang and Faeth[68] computed the drag

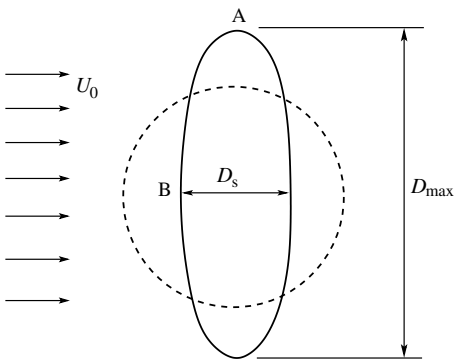

Figure 3: Schematic of the drop deformation quasi-static model for estimating D_{max}/D_0.

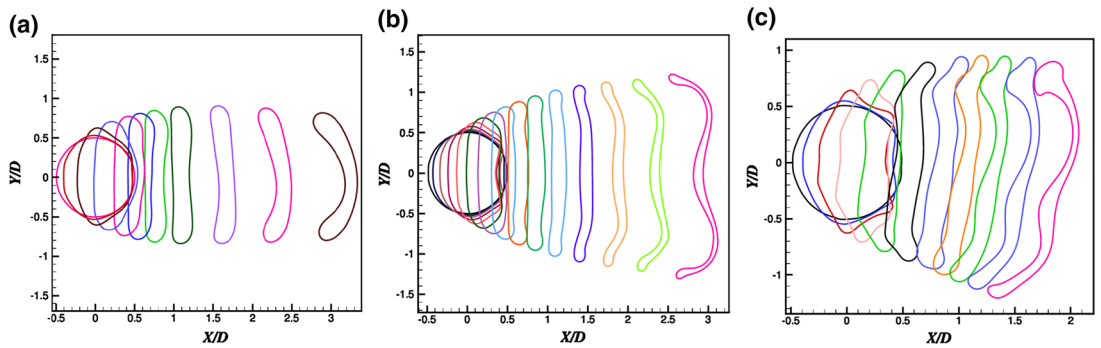

Figure 2: Drop shape evolution for $Re_l = 1414$ and **a** Bag breakup at $We = 20$, **b** Bag-with-stamen breakup at $We = 40$ and **c** $We = 80$. (reprinted from Jain et al.[13] with permission of R Soc Proc A).

Table 3: D_{max}/D_0 as a function of We[13].

We	D_{max}/D_0 from Eq. (16)	D_{max}/D_0 simulations in[13]	D_{max}/D_0 from Eq. 8 in[68]
20	1.81	1.80	1.85
40	2.09	2.15	2.20
80	2.40	2.2	2.70

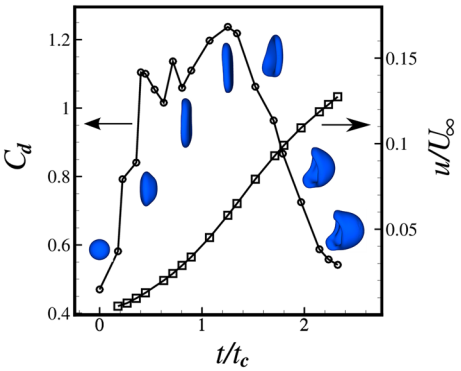

Figure 4: Drag coefficient for the deforming drop as a function of time for $We = 20$ (reprinted from Jain et al.[13] with permission of R Soc Proc A).

coefficient using the measurements of the centroid and presented it as a function of the diameter in the cross-streamwise direction. The drag coefficient varies from that for a solid sphere ($\sim$ 0.424) to that for a solid disk ($\sim$ 1.2). Jain et al.[13] presented a similar calculation from the simulation which agrees well with the experiments of Hsiang and Faeth[68]. Once the drag coefficient reaches a maximum value, the drop starts forming a bag and drag coefficient decreases due to a decrease in the relative velocity (see Fig. 4).

The time scale for initial deformation is governed by the capillary velocity. In the inertial regime, the capillary velocity is governed by $U_{\text{capillary}} = (\sigma/\rho_l L)^{1/2}$, where L is the characteristic length scale. In the viscous regime the capillary velocity is given by $U_{\text{capilary}} = \sigma/\mu_l$. Based on these velocities, the ratio of the capillary to the characteristic time scale for the deformation to travel across the deformed droplet can be written as $\sqrt{2We_a\rho_g/\rho_l}$ and $Oh_l\sqrt{We}$, respectively. For $Oh_l = 0.1$ and $We = 20$, the ratio based on the viscous capillary time scale is $\sim$ 0.90 which is in better agreement with the observations in simulations of Jain et al.[13] ($\sim$ 1). Thus, we can conclude that although the aerodynamic Weber number is high ($\sim$ 20–80), the capillary waves at these Weber numbers are governed by the slower viscous timescales based on liquid viscosity. Time scale for complete breakup has been proposed to be $5t_c$ independent of We[35, 68, 70, 71]. Hsiang and Faeth[68] proposed the following correlation for the breakup time scale:

$$t_{bu}/t_c = 5/(1 - Oh_l/7). \tag{17}$$

It has a weak dependence on Oh_l but for $Oh_l < 0.1$ it can be assumed to be a constant. In simulations, however, time for breakup is < 3.0 due to an early numerical breakup of the bag. To capture the entire breakup accurately in simulations, bag growth as it thins needs to be captured using an extremely fine grid which makes the simulation impractical. Moreover, intermolecular forces that become active as the bag becomes less than a micron thinner in certain regions should be modeled. For the complicated shape of the bag, to estimate intermolecular forces is difficult and, therefore, has not been incorporated in simulations yet. Nevertheless, in near future multiscale modeling techniques are expected to resolve such issues.

4 Breakup Modes

With increase in Weber number the droplet deformation and breakup mode undergoes continuous change. For Weber numbers $We < 6$, surface tension can resist breakup. Vibrational breakup is expected for a $We < 12$. The external flow leads to oscillations of the drop and as the amplitude of the oscillations grows the droplet may breakup into a few fragments. TAB model used extensively in Lagrangian Spray modeling essentially captures only the vibrational breakup. For $We > 12$, bag breakup mode is expected, where after the initial deformation, the disk shaped droplet is inflated into a balloon shaped bag held together by a thicker rim. For higher We, interesting features appear on the bag such as stamen in the center of the bag and multiple connected lobes attached to each other with thicker liquid threads and all these threads are attached to a central rim (see Jain et al.[13] for detailed of the bag shapes). At $We > 80$, a significant change in the breakup mode occurs, where the rim of the disk shaped drop, formed after the initial deformation, stretches in the direction of the flow thus resulting in a backward facing bag. At even higher We, the nature of the initial deformation of the droplet also undergoes a change. The drop as it deforms is subjected to Kelvin–Helmholtz instability resulting in a rough windward surface that continuously ejects tiny droplets. The initial phase also involves stripping of drops from

the periphery of the droplet but at later times the entire droplet suddenly breakups into tiny fragments[37]. Joseph et al.[39] argued that the Rayleigh–Taylor instability leads to the sudden fragmentation of the droplet. The waviness of the windward surface observed in shadowgraphs (see Figure 11 in Liu and Reitz[45]) also indicates the presence of an instability. There have been some simulations of the catastrophic breakup using compressible–compressible formulations[72], where the initial droplet deformation and the flow structures forming behind the droplet were captured. At moderate Weber numbers, most simulations have been performed at low-density ratios that result in dynamics which is quite different from the one observed in experiments. Jain et al.[13] presented simulations at high-density ratio and captured the bag, bag and stamen, and shear breakup.

In what follows, we discuss the transition Weber numbers for different modes of breakup and also the effect of various parameters, such as liquid/gas density ratio and gas Reynolds number, on the transition Weber number.

5 Transition Weber Numbers

The previous sections discussed the various breakup regimes of the spherical liquid droplet when it interacts with different magnitudes of air stream velocities. In this section we shall focus more on the Weber numbers associated with these regimes and the transition regions.

Weber number is one of the most important parameters associated with secondary breakup. It captures the interplay of inertial and surface tension forces. The drop being initially stationary and the exchange of the moment at the outer surface of the liquid occurs through viscous forces; therefore, liquid Ohnesorge number is required to estimate the importance of viscous forces. One of the first attempts to capture the viscous forces in this context was made by Hinze[5]. Experimental observations of breakup of a single drop show that the spherical droplet undergoes deformation into various interesting shapes (as discussed in the previous sections). While the physics of these processes have not been entirely understood yet, the initial deformation of the drop is also equally interesting and has not been looked into in detail in the literature. One may easily notice that for a given experimental setup (including liquid and its drop size) aerodynamic Weber number, *We*, acts as a direct function of the relative velocity between the droplet and the freestream air. When this relative velocity is not present ($We = 0$), the liquid droplet is stable in its spherical shape. When a relative velocity is established between the droplet and the ambient gas medium, the inertial forces may cause deformation and instabilities on the droplet surface and may eventually lead to breakup of the drop. However, at low speeds, the droplet only vibrates and does not disintegrate till the relative velocity and effectively the *We* crosses a certain threshold. This first barrier is termed as the critical Weber number and may be defined as the minimum Weber number required for the liquid droplet to undergo breakup. The critical Weber number is generally agreed upon in the literature to lie between 10 and 12 for $Oh_l \ll 1$. We would like to note here that the condition posed for the Ohnesorge number limits the critical Weber number to low viscosity fluids. However, there have been attempts earlier to relate the critical Weber number and liquid Ohnesorge number, for instance, Brodkey[18] proposed a correlation (see Eq. 1) which was subsequently verified by Pilch and Erdman[7] (see Fig. 1).

Recently, Theofanous et al.[11,72,73] have studied the breakup of viscous liquids in greater detail. Theofanous et al. debunk the claim made in the literature that the droplet does not at all undergo breakup with increasing magnitudes of Oh_l. It is rather argued that the deformation time scales increase and during the initial deformation phase itself the droplet accelerates to higher velocities. With the reduction in the relative velocity, the high-viscosity droplet 'misses the window of opportunity' to disintegrate further. However, it is also mentioned that as the droplet accelerates it experiences the effects of RT instability, but just not for long enough to cause disintegration. It has been established that for liquids with $Oh_l < 0.1$, i.e., low enough viscous forces when compared to inertial and surface tension forces, the regimes of secondary breakup solely depend on *We*. To put things within a broader perspective, while it is known that the drop breakup regimes follow established rules of transition with Weber numbers for low viscosities ($Oh_l \ll 1$), the viscous drop breakup is yet to be understood.

The important aspect to note here is the consideration of the dominant instability mechanisms that dictate these modes of breakup. Rayleigh–Taylor instability is said to dominate the immediate regimes at Weber number greater than the critical Weber number. With increasing magnitudes of *We*, the Kelvin–Helmholtz mode of instability begin to dominate the deformation of the droplet. While RT instability is characterized by the formation of bags, KH instability manifests itself during the initial phase of the

catastrophic breakup. Nevertheless, the final deformation is subjected to RT instability in the catastrophic breakup (see Joseph et al.[39]). Shear stripping mode can be seen as a transition from RT instability to shear forces becoming dominant and stretching the edge of the droplet towards the direction of flow thus hindering the formation of the bag[13]. The common occurrence across all the regimes is the initial deformation, where a spherical drop undergoes flattening and becomes a flat disk-like structure before going through any mode of breakup. Though there have been attempts to capture the physics of breakup structures viz. bag breakup and bag-stamen breakup, there is still scope to analyse further the initial deformation (sphere to flat-disk) dynamics to possibly reveal more details on the exact nature and cause of the different regimes. Due to the limitations of experiments, numerical efforts are crucial in understanding this very aspect of the secondary breakup process. Computational methods have evolved significantly over the last decade to now enable the simulation of the entire drop breakup process at realistic density ratios (1000 : 1 for water–air systems). These may be termed as numerical experiments in the sense of being quite close to the actual experiments in setup. The recent works[13, 16] have been able to capture the complex modes involving bag, bag-stamen, multi-bag and also the shear stripping breakup regimes. Such data obtained from simulations aids us by providing much more information than one could obtain through experiments.

Mohit et al.[13] conducted volume-of-fluid-based three-dimensional simulations to capture secondary breakup at high-density ratios. The Weber numbers ranged from 20 to 120 covering all the breakup regimes (except for catastrophic breakup), namely, bag breakup, bag and stamen breakup, multi-bag breakup and shear stripping breakup. These simulations were carried out to mimic the experiments, where droplets are introduced into a continuous air stream. The breakup structures, the deformation time scale and the breakup times matched favourably with the experimental data. The multi-bag breakup regime which is not often reported even in the experimental literature ($55 < We < 75$; see Cao et al.[74]) is captured with all the physical structures involved in the formation of multiple bags instead of a single bag interconnected by thicker rim-like strips of liquid and the outer thicker rim holding everything in place till further disintegration. The transition of regimes from bag breakup, where the RT instability dominates, till the changeover to shear breakup is primarily attributed to rim dynamics. Figure 5 shows the snapshots of multi-bag breakup at various time instances in terms of the characteristic time. The experiments shown here are reported in[75].

It is being increasingly agreed upon that the deformation dynamics of the spherical droplet before the beginning of the process of breaking up affects the final distribution of fine droplets and their velocities. Therefore, it is imperative for the numerical simulations also to capture this aspect as accurately as possible. One of the vital parameters that is an indicator of this phenomena is the ratio D/D_0 of the deforming droplet. The simulations by Jain et al.[13] reportedly captured this behaviour matching well with the experimental results already available in the previous literature[14, 74, 76].

The transition of bag breakup regimes to shear breakup regimes happens due to the nature of rim dynamics. This transition manifests itself around $We \sim 100$ and all the preceding regimes involving bag structures are known to be influenced by the RT instability, where the bulk of the liquid is also pierced through by the air stream. The shear breakup on the other hand, while being dominated by KH instabilities, involves the air stream flowing around the droplet causing rapid disintegration of the bulk of the droplet. The transition itself is reported to happen due to the surface tension effects and the associated rim dynamics. The rim may be identified as the prominent structure that is absolutely essential to not just hold the bag but also to allow the formation of all the bag structures for $We < 80$. The velocity of the rim retraction in the simulations agree well with the theoretical values of the Culick velocity obtained for an average film thickness of the bag. At high Weber numbers the shear forces drag along the rim and lead to stretching of the periphery of the drop in the streamwise direction thus resulting in a backward facing bag with streaming of drop from the periphery. Whereas, for lower Weber numbers rim shows a tendency of getting sheared by the flow but upon subsequent deformation retracts back leading to the formation of a more circular and stable rim. This behaviour is well reflected in the Figure 14 of Ref.[13], showing the central plane cut section of the deforming droplet at $We = 80$.

Effect of density ratio on the breakup modes has not been studied well. There have been a few studies, where the effect of density ratio has been discussed to a certain extent. However, in experimental studies, only either low-density ratios 1–10 or higher density ratio > 800 systems have been studied. Most numerical studies have been

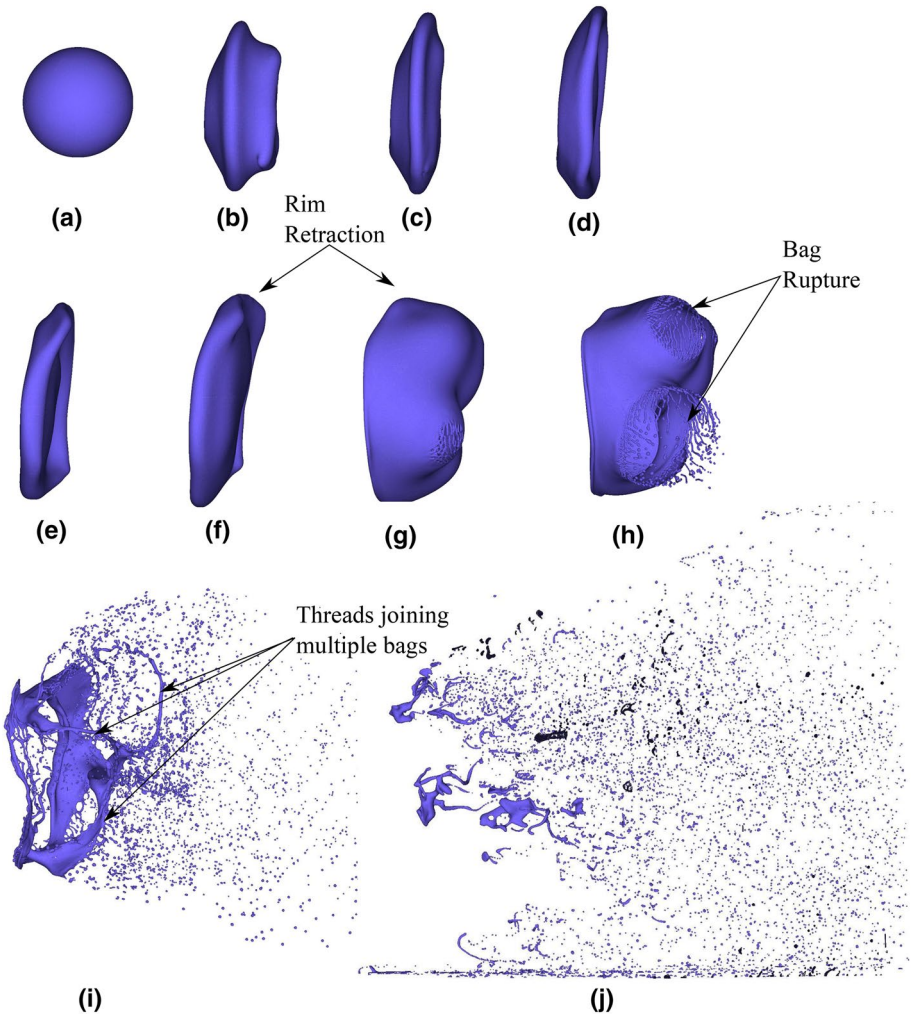

Figure 5: Snapshots from numerical simulations showing the structure of the disintegrating droplet for $We = 80$ at different times: t/t_c **a** 0, **b** 0.54, **c** 0.71, **d** 0.89, **e** 1.20, **f** 1.38, **g** 1.65, **h** 1.74, **i** 1.96, **j** 2.77.

performed at lower density ratio < 100[15, 17, 19, 20, 22, 77, 78]. Only recently, a few studies have been performed for the higher density ratio ~ 1000[13, 16, 72, 79]. In a recent study, Suhas et al.[79] carried out a parametric study with a focus on density ratio to bridge this gap in understanding by conducting 2-D axisymmetric numerical simulations and supplementing them with three-dimensional simulations. The focus of this work was to study the deformation dynamics of the drop only up to the onset of breakup, and thus only to identify the mode of breakup and not the complete breakup, and therefore, 2-D axisymmetric treatment was sufficient. The study spanned the density ratios starting from as low as 10 all the way up to 1000 and Weber numbers ranging from 20 to 120. We would like emphasize here that the Ohnesorge number was still low ($Oh_l \sim 0.1$; $Oh_l \ll 1$). The time taken by the droplets to evolve in shape was closely investigated at different density ratios, DR. The time is non-dimensionalized with the characteristic time scale, $t* = t/t_c$. Figure 6 shows the time evolution of the drop shape and the displacement for $DR = 10$ and $DR = 1000$ at $We = 20$. The flow of the gas is from left to

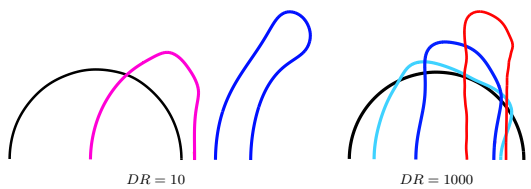

Figure 6: Comparison of the deformation shapes of the drop evolving in time for $DR = 10$ and $DR = 1000$ at $We = 20$.

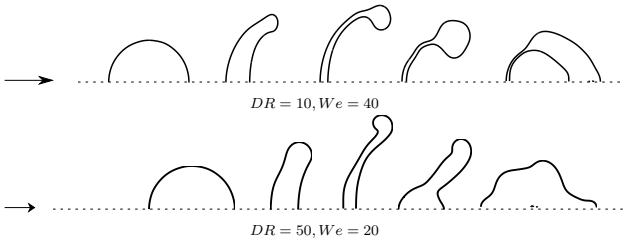

Figure 7: Deforming drops evolving in time (space in between does not show the actual movement) for $DR = 10$ at $We = 20$, 40 and $DR = 50$ at $We = 20$. Dotted lines mark the axis of symmetry. These conditions do not exhibit any breakup of the droplets.

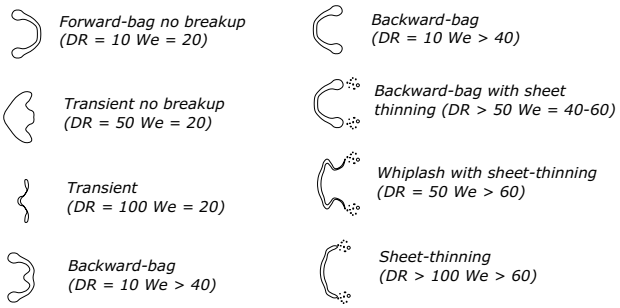

Figure 8: Phase plot *DR*–*We* along with the typical drop shapes for breakup modes shown on the right. Hatched region shows the transition regime. The *DR* axis is scaled to the logarithm base of 2.

right. Centroid of the drop for $DR = 10$ moves a distance of $0.79d0$, for $DR = 200$ drop moves a distance of $0.48D_0$ (not shown in the figure) and for $DR = 1000$ the drop moves a distance of $0.34D_0$ in a timespan of $t* = 1$. The leeward side of the drop for $DR = 10$ also moves downstream with time, whereas the leeward side of the drop for $DR = 1000$ remains virtually stationary until $t* = 1$, though the centroid is moving in the streamwise direction in both the cases. The significant difference in the motion of the centroid is primarily due to the differences in the velocity of the drop and the rate of momentum transmitted to the leeward side of the drop, which depends on

Table 4: Typical shapes of the drop at the onset of breakup for $\boldsymbol{DR} =$ 50, 150 and 1000 at $\boldsymbol{We} =$ 20 60 and 120, $\boldsymbol{Re_g = 4000}$, $\boldsymbol{M = 100}$ and $\boldsymbol{Oh} =$ 0.003–0.9.

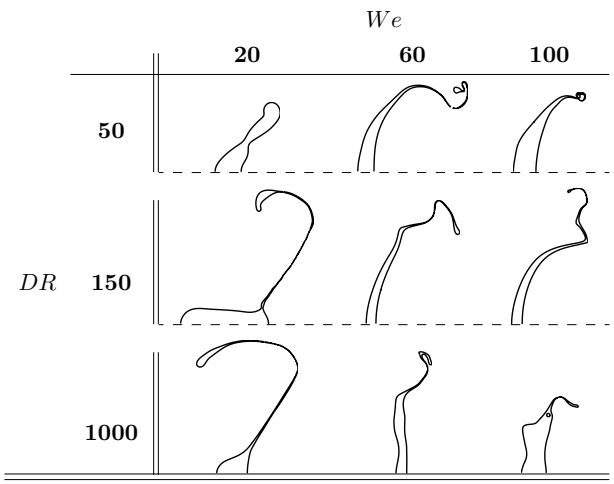

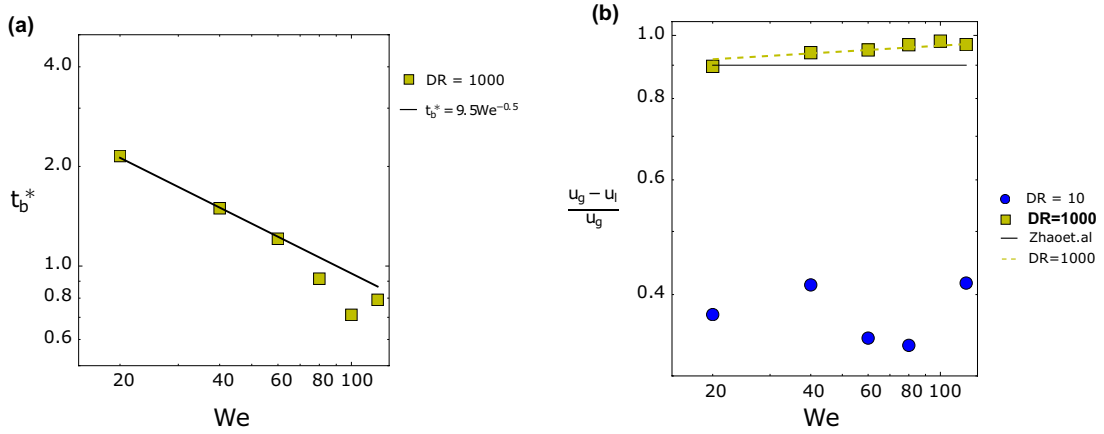

Figure 9: For $DR = 1000$: **a** time at the onset of breakup. Solid line represents the power law fit. **b** Relative velocity at the onset of breakup. Solid line represents the results by[80]. Dotted line shows the general power law fit[79].

the kinematic viscosity. Combined effects of capillary (Rayleigh) time scales and the rim-stretching time scales results in the formation of 'reverse bag-like' structure, that does not disintegrate further. Figure 7 shows the conditions, where the droplet do not undergo any breakup which are also in agreement with the low-density simulations of Han and Tryggvason[20, 78]. This is attributed to the instantaneous Weber numbers, which falls below the We_c, since the drops at low DR accelerate faster due to higher values of kinematic viscosity, an argument similar to the one used for very viscous droplets.

To study the morphology of the drops during breakup, typical shapes of the drops at the onset of the breakup have been tabulated in Table 4 for all the conditions. To summarize the breakup modes presented in this table, typical characteristic shapes are drawn, as shown in Fig. 8.

In addition to these differences in the deformation, breakup morphologies and breakup modes, the breakup mechanism is also different for higher and lower DR values. Breakup is due to the RT instability at higher DR values ($DR > 150$)[13, 41, 79], whereas breakup is due to the dynamics of the rim at lower DR values and is significantly influenced by the surrounding gas flow[79]. Hence, drops for roughly $DR > 150$ behave similarly at similar values of We. This difference in breakup for different DR values (other non-dimensional parameters being constant $Oh_l < 0.1$) makes "Density Ratio" a crucial parameter in characterizing the secondary breakup of drops.

Figure 9 shows the drop breakup time and the relative velocity of the centroid of the drop, respectively, at the onset of breakup. The drop breakup time are quite different for the drops with $DR = 10$ and for the drops with $DR = 50 - 1000$. With an increase in We, breakup time decrease following the power law given by $t_b = 9.5We^{-0.5}$. Relative velocity on the other hand has a continuous variation from $DR = 50$ to $DR = 1000$ following a general power law given by $4(10{-}4\rho_l + 0.1)We^{(0.13-10^{-4}\rho_l)}$ with average values increasing from 0.76 to 0.95, though it is significantly different for $DR = 10$ with an average value of 0.36. Zhao et al.[76] reported an average value of 0.9 for ethanol and water drops combined which is in good agreement with simulations in[79] and experimental value of 0.87 for water drops in Dai and Faeth[41]. Relative velocity increases with an increase in DR value indicating that the drops for lower DR would attain higher velocity at the onset of breakup. Jain et al.[79] report that the drops for $DR = 10$ at $We = 20$ and 40 and for $DR = 50$ at $We = 20$, do not breakup at all. This is in good agreement with the observations of Han and Tryggvason[20].

6 Summary

We presented a brief review of the experimental and numerical investigations of secondary breakup of liquid drops. Although several experimental studies have been carried out in the last few decades, a comprehensive understanding of the mechanisms involved in the breakup process still alludes us. Secondary breakup of a drop is short time phenomenon lasting a few micro seconds and the flow structures around the drop during breakup are difficult to capture in experiments. The recent developments in the

algorithms of two-phase flow simulations has made the simulations of drop breakup possible. However, to capture the complete breakup the bag needs to be resolved up to sub-micron level which requires extremely refined grids. Therefore, accurate robust simulations up to the breakup of the bag become impractical and in the literature an early breakup is reported. It is expected that multiscale schemes would resolve such issues.

In the secondary atomization literature, significant attention has been paid to the breakup modes but the initial deformation of the drop have been not so well studied. Although, there have been some studies on the time scales of initial deformation and also displacement of the droplet in the initial phase of deformation, lack of information on flow structures behind the deforming drops from experiments limits the physical understanding of exact mechanisms. Robust accurate numerical simulations can fill this gap and thereby assist in gaining insight into the exact physical mechanisms involved in the secondary atomization at different Weber numbers.

It has been believed that at low liquid Ohnesorge numbers (less that 0.1), the aerodynamic Weber number alone determines the breakup mode. However, recent simulations indicate that density ratio as well as the gas Reynolds number play a significant role in breakup mode selection. Similarly, it has been observed that non-Newtonian and viscoelastic fluids affect the critical Weber numbers required for transition from one breakup regime to another[81]. Similarly, breakup of drops of nano-particle colloidal solutions and other suspensions can be expected to be substantially different from that of the pure fluids[82].

Acknowledgements

Authors would like to thank Suhas S. Jain (Stanford Univ.) for many useful discussions.

Received: 30 August 2018 Accepted: 17 September 2018
Published online: 16 October 2018

References

1. Wu PK, Ruff G, Faeth GM (1991) Primary breakup in liquid–gas mixing layers. At Sprays 1(4):421
2. Wu PK, Tseng LK, Faeth GM (1992) Primary breakup in gas/liquids mixing layers for turbulent liquids. At Sprays 2(3):295
3. Hall DW (1980) A detailed microphysical model within a two-dimensional dynamic framework: model description and preliminary results. J Atmos Sci 37:2486
4. Villermaux E, Bossa B (2010) Size distribution of raindrops. Nat Phys 6:232
5. Hinze J (1955) Fundamentals of the hydrodynamic mechanism of splitting in dispersion processes. AIChE J 1(3):289
6. Engel O (1958) Fragmentation of waterdrops in the zone behind an air shock. J Res Natl Bur Stand 60(3):245
7. Pilch M, Erdman C (1987) Use of breakup time data and velocity history data to predict the maximum size of stable fragments for acceleration-induced breakup of a liquid drop. Int J Multiph Flow 13(6):741
8. Krzeczkowski SA (1980) Measurement of liquid droplet disintegration mechanisms. Int J Multiph Flow 6(3):227
9. Hsiang LP, Faeth G (1995) Drop deformation and breakup due to shock wave and steady disturbances. Int J Multiph Flow 21(4):545
10. Guildenbecher RD (2009) Secondary atomization. Exp Fluids 46:371–402
11. Theofanous T (2011) Aerobreakup of Newtonian and viscoelastic liquids. Annu Rev Fluid Mech 43(1):661
12. Chou WH, Hsiang LP, Faeth G (1997) Temporal properties of drop breakup in the shear breakup regime. Int J Multiph Flow 23(4):651
13. Jain M, Prakash RS, Tomar G, Ravikrishna RV (2015) Secondary breakup of a drop at moderate Weber numbers. Proc R Soc A Math Phys Eng Sci 471(2177):20140930
14. Chou WH, Faeth G (1998) Temporal properties of secondary drop breakup in the bag breakup regime. Int J Multiph Flow 24(6):889
15. Khosla S, Smith CE, Throckmorton RP (2006) Detailed understanding of drop atomization by gas crossflow using the volume of fluid method. In: ILASS Americas, 19th annual conference on liquid atomization and spray systems, Toronto, Canada
16. Xiao F, Dianat M, McGuirk JJ (2014) Large eddy simulation of single droplet and liquid jet primary breakup using a coupled level set/volume of fluid method. At Sprays 24(4):281
17. Jalaal M, Mehravaran K (2012) Fragmentation of falling liquid droplets in bag breakup mode. Int J Multiph Flow 47:115
18. Brodkey R (1967) The phenomena of fluid motions. Addison-Wesley, Reading Google Scholar, Boston
19. Zaleski S, Li J, Succi S (1995) Two-dimensional Navier–Stokes simulation of deformation and breakup of liquid patches. Phys Rev Lett 75:244
20. Han J, Tryggvason G (2001) Secondary breakup of axisymmetric liquid drops. II. Impulsive accelerationSecondary breakup of axisymmetric liquid drops. II. Impulsive acceleration. Phys Fluids 13(6):1554
21. Kékesi T, Amberg G, Wittberg LP (2014) Drop deformation and breakup. Int J Multiph Flow 66:1
22. Jalaal M, Mehravaran K (2014) Transient growth of droplet instabilities in a stream. Phys Fluids 26(1):012101
23. Patel PD, Theofanous TG (1981) Hydrodynamic fragmentation of drops. J Fluid Mech 103:207
24. Simpkins PG, Bales EL (1972) Water-drop response to sudden accelerations. J Fluid Mech 55:629

25. Harper EY, Grube GW, Chang ID (1972) On the breakup of accelerating liquid drops. J Fluid Mech 52(3):565
26. Rumscheidt F, Mason S (1961) Particle motions in sheared suspensions XII. Deformation and burst of fluid drops in shear and hyperbolic flow. J Colloid Sci 16(3):238
27. Kennedy M, Pozrikidis C, Skalak R (1994) Motion and deformation of liquid drops, and the rheology of dilute emulsions in simple shear flow. Comput Fluids 23(2):251
28. Bentley BJ, Leal LG (1986) An experimental investigation of drop deformation and breakup in steady, two-dimensional linear flows. J Fluid Mech 167:241283
29. Villermaux E (2007) Fragmentation. Annu Rev Fluid Mech 39(1):419
30. Montero-Martnez G, Kostinski AB, Shaw RA, Garca-Garca F (2009) Do all raindrops fall at terminal speed? Geophys Res Lett 36:11
31. Faeth G (1996) Spray combustion phenomena. Symp (Int) Combust 26(1):1593
32. Rizk N, Lefebvre A (1984) Spray characteristics of plain-jet airblast atomizers. ASME J Eng Gas Turbines Power 106(3):634
33. Rao DC, Karmakar S, Basu S (2017) Atomization characteristics and instabilities in the combustion of multicomponent fuel droplets with high volatility differential. Sci Rep 7:8925
34. Taylor GI (1963) The shape and acceleration of a drop in a high speed air stream. Sci Pap G I Taylor 3:457
35. Ranger AA, Nicholls JA (1969) Aerodynamic shattering of liquid drops. AIAA J 7:285
36. Gelfand B (1996) Droplet breakup phenomena in flows with velocity lag. Progress Energy Combust Sci 22(3):201
37. Wierzba A, Takayama K (1988) Experimental investigation of the aerodynamic breakup of liquid drops. AIAA J 26:1329
38. Faeth G, Hsiang LP, Wu PK (1995) Annual reviews in multiphase flow 1995 structure and breakup properties of sprays. Int J Multiph Flow 21:99
39. Joseph DD, Belanger J, Beavers GS (1999) Breakup of a liquid drop suddenly exposed to a high-speed airstream. Int J Multiph Flow 25:1263
40. Igra D, Takayama K (2001) Numerical simulation of shock wave interaction with a water column. Shock Waves 11(3):219
41. Dai Z, Faeth G (2001) Temporal properties of secondary drop breakup in the multimode breakup regime. Int J Multiph Flow 27(2):217
42. Theofanous TG, Li GJ, Dinh TN (2004) Aerobreakup in rarefied supersonic gas flows. J Fluid Eng T ASME 126:516527
43. Liu AB, Reitz RD (1993) Mechanisms of air-assisted liquid atomization. At Sprays 3(1):55
44. Hwang S, Liu Z, Reitz RD (1996) Breakup mechanisms and drag coefficients of high-speed vaporizing liquid drops. At Sprays 6(3):353
45. Liu Z, Reitz R (1997) An analysis of the distortion and breakup mechanisms of high speed liquid drops. Int J Multiph Flow 23(4):631
46. Flock A, Guildenbecher D, Chen J, Sojka P, Bauer HJ (2012) Experimental statistics of droplet trajectory and air flow during aerodynamic fragmentation of liquid drops. Int J Multiph Flow 47:37
47. Vieille B, Chauveau C, Gökalp I (1997) Droplet breakup regimes under high pressure conditions. AIAA J 98:0715
48. O'Rourke PJ, Amsden AA (1987) The tab method for numerical calculation of spray droplet breakup. In: SAE technical paper (SAE International)
49. Clark MM (1988) Drop breakup in a turbulent flow-I. Conceptual and modeling considerations. Chem Eng Sci 43(3):671
50. Ibrahim EA, Yang H, Przekwas A (1993) Modeling of spray droplets deformation and breakup. J Propuls Power 9(4):651
51. Park JH, Yoon Y, Hwang SS (2002) Improved TAB model for prediction of spray droplet deformation and breakup. At Sprays 12(4):387
52. Lee MW, Park JJ, Farid MM, Yoon SS (2012) Comparison and correction of the drop breakup models for stochastic dilute spray flow. Appl Math Modell 36(9):4512
53. Schmehl R (2002) Advanced modeling of droplet deformation and breakup for CFD analysis of mixture preparation. In: ILASS Europe, 18th annual conference on liquid atomization and spray systems, Zaragosa, Spain
54. Reitz RD, Diwakar R (1987) Structure of high-pressure fuel sprays. In: SAE technical paper (SAE International)
55. Chryssakis C, Assanis DN (2005) A Secondary atomization model for liquid droplet deformation and breakup under high Weber number conditions. In: ILASS Americas, 18th annual conference on liquid atomization and spray systems, Irvine, CA, USA
56. Reitz R (1987) Mechanisms of atomization processes in high-pressure vaporizing sprays. At Spray Technol 3(4):309
57. Tanner FX (1997) Liquid jet atomization and droplet breakup modeling of non-evaporating diesel fuel sprays. In: SAE technical paper (SAE International)
58. Tanner FX (2004) Development and validation of a cascade atomization and drop breakup model for high-velocity dense sprays. At Sprays 14:3
59. Apte S, Gorokhovski M, Moin P (2003) LES of atomizing spray with stochastic modeling of secondary breakup. Int J Multiph Flow 29(9):1503
60. Apte S, Mahesh K, Moin P, Oefelein J (2003) Large-eddy simulation of swirling particle-laden flows in a coaxial-jet combustorLarge-eddy simulation of swirling particle-laden flows in a coaxial-jet combustor. Int J Multiph Flow 29(8):1311
61. Sichani AB, Emami MD (2015) A droplet deformation and breakup model based on virtual work principle. Phys Fluids 27(3):032103
62. Brackbill J, Kothe D, Zemach C (1992) A continuum method for modeling surface tension. J Comput Phys 100(2):335
63. Popinet S (2009) An accurate adaptive solver for surface-tension-driven interfacial flows. J Comput Phys 228(16):5838

64. Popinet S (2018) Numerical models of surface tension. Annu Rev Fluid Mech 50(1):49
65. Tomar G, Fuster D, Zaleski S, Popinet S (2010) Multi-scale simulations of primary atomization. Comput Fluids 39(10):1864
66. Popinet S (2003) Gerris: a tree-based adaptive solver for the incompressible Euler equations in complex geometries. J Comput Phys 190(2):572
67. Lee CH, Reitz RD (2000) An experimental study of the effect of gas density on the distortion and breakup mechanism of drops in high speed gas stream. Int J Multiph Flow 26:229
68. Hsiang LP, Faeth G (1992) Near-limit drop deformation and secondary breakup. Int J Multiph Flow 18(5):635
69. Baines M (1979) Hydrodynamic fragmentation in a dense dispersion. In: Proceedings of 4th CSNI specialists meeting on fuel-coolant interactions in nuclear reactor safety, 2–5 April, Bournemouth, UK
70. Reinecke WG, McKay WL (1969) Experiments on water-drop breakup behind Mach 3 to 12 shocks. In: Sandia Corp. Report SC-CR-70-6063
71. Reinecke WG, Waldman GD (1970) A study of drop breakup behind strong shocks with applications to flight. In: Avco Report AVSD-0110-70-77
72. Theofanous T, Mitkin V, Ng C, Chang C, Deng X, Sushchikh S (2012) The physics of aerobreakup. II. Viscous liquids. Phys Fluids 24(2):022104
73. Theofanous T, Li G (2008) On the physics of aerobreakup. Phys Fluids 20(5):052103
74. Cao XK, Sun ZG, Li WF, Liu HF, Yu ZH (2007) A new breakup regime of liquid drops identified in a continuous and uniform air jet flow. Phys Fluids 19(5):057103
75. Surya Prakash R (2018) Liquid jet in swirling cross flow. Ph.D. Thesis, Indian Institute of Science Bangalore
76. Zhao H, Liu HF, Xu JL, Li WF, Lin KF (2013) Liquid jet in swirling cross flow. Phys Fluids 25(5):054102
77. Kekési T (2017) Scenarios of drop deformation and breakup in sprays. Scenarios of drop deformation and breakup in sprays. Ph.D. Thesis, The Royal Institute of Technology, Stockholm, Sweden
78. Han J, Tryggvason G (1999) Secondary breakup of axisymmetric liquid drops. I. Acceleration by a constant body force. Phys Fluids 11(12):3650
79. Jain SS, Suryaprakash R, Raghunandan B, Ravikrishna R, Tomar G (2018) Effect of density ratio on the secondary breakup: a numerical study **(under review)**
80. Zhao H, Liu HF, Li WF, Xu JL (2010) Morphological classification of low viscosity drop bag breakup in a continuous air jet stream. Phys Fluids 22(11):114103
81. Theofanous TG, Mitkin VV, Ng CL (2013) The physics of aerobreakup III. Viscoelastic liquids. Phys Fluids 25(3):032101
82. Pathak B, Basu S (2016) Phenomenology of break-up modes in contact free externally heated nanoparticle laden fuel droplets. Phys Fluids 28(12):123302

Dr. R. Suryaprakash is currently working as a research associate in the department of Mechanical Engineering, Indian Institute of Science. He completed his Masters and PhD from the department of Aerospace Engineering at the Indian Institute of Science in 2012 and 2018, respectively. His areas of research interest are experimental and numerical investigations of atomization and sprays of liquid fuels.

Dr. Gaurav Tomar is currently an Associate Professor in the Department of Mechanical engineering at Indian Institute of Science, Bangalore. He completed his Bachelor's and PhD from the Indian Institute of Technology, Kanpur, in 2003 and 2008, respectively. Before joining the Indian Institute of Science in 2010 as an Assistant Professor, he worked as a postdoctoral fellow in the University of Pierre et Marie Curie, Paris, and University of California Santa Barbara, USA. His research interests are in the area of numerical simulations of multiphase phenomena including boiling, sprays and bubble formation.